



Sun, R. (2017). 3D Tunable, Multiscale, and Multistable Vibrational Micro-Platforms Assembled by Compressive Buckling. *Advanced Functional Materials*, 27(22). <https://doi.org/10.1002/adfm.201605914>

Peer reviewed version

Link to published version (if available):
[10.1002/adfm.201605914](https://doi.org/10.1002/adfm.201605914)

[Link to publication record in Explore Bristol Research](#)
PDF-document

This is the author accepted manuscript (AAM). The final published version (version of record) is available online via *Advanced Functional Materials* at <http://onlinelibrary.wiley.com/doi/10.1002/adfm.201605914/abstract>. Please refer to any applicable terms of use of the publisher.

University of Bristol - Explore Bristol Research

General rights

This document is made available in accordance with publisher policies. Please cite only the published version using the reference above. Full terms of use are available:
<http://www.bristol.ac.uk/pure/about/ebr-terms>

DOI: 10.1002/ ((please add manuscript number))

Article type: Full Paper

Three-Dimensional Multiscale, Multistable, and Geometrically Diverse Microstructures with Tunable Vibrational Dynamics Assembled by Compressive Buckling

Xin Ning[†], Heling Wang[†], Xinge Yu[†], Julio A. N. T. Soares, Zheng Yan, Kewang Nan, Gabriel Velarde, Yeguang Xue, Rujie Sun, Qiyi Dong, Haiwen Luan, Chan Mi Lee, Aditya Chempakasseril, Mengdi Han, Yiqi Wang, Luming Li, Yonggang Huang, Yihui Zhang, John Rogers**

[*] Prof. John A. Rogers, Corresponding-Author

Department of Materials Science and Engineering, Biomedical Engineering, Neurological Surgery, Chemistry, Mechanical Engineering, Electrical Engineering and Computer Science
Simpson Querrey Institute and Feinberg Medical School
Center for Bio-Integrated Electronics
Northwestern University
Evanston, Illinois 60208 (USA)
E-mail: jrogers@northwestern.edu

[*] Prof. Yihui Zhang, Corresponding-Author

Center for Mechanics and Materials, AML, Department of Engineering Mechanics,
Tsinghua University
Beijing 100084 (P.R. China)
E-mail: yihuizhang@tsinghua.edu.cn

Dr. Xin Ning, Dr. Xinge Yu, Dr. Julio A.N.T. Soares, Dr. Zheng Yan, Mr. Kewang Nan, Mr. Gabriel Velarde, Mr. Yiqi Wang
Department of Materials Science and Engineering
Frederick Seitz Materials Research Laboratory
University of Illinois at Urbana-Champaign
Urbana, Illinois 61801 (USA)

Mr. Rujie Sun
Advanced Composites Centre for Innovation and Science,
University of Bristol
Bristol, BS8 1TR (UK)

Dr. Heling Wang, Mr. Yeguang Xue, Mr. Haiwen Luan
Departments of Civil and Environmental Engineering, and Mechanical Engineering
Northwestern University
Evanston, Illinois 60208 (USA)

Mr. Qiyi Dong
Department of Industrial and Enterprise Systems Engineering
University of Illinois at Urbana-Champaign
Urbana, Illinois 61801 (USA)

Ms. Chan Mi Lee
Department of Chemistry
University of Illinois at Urbana-Champaign

Urbana, Illinois 61801 (USA)

Mr. Aditya Chempakasseril
Department of Chemical and Biomolecular Engineering
University of Illinois at Urbana-Champaign
Urbana, Illinois 61801 (USA)

Mr. Mengdi Han
National Key Laboratory of Science and Technology on Micro/Nano Fabrication,
Peking University, Beijing 100871 (P.R. China)

Prof. Luming Li
Man-machine-Environment Engineering Institute, Department of Aeronautics & Astronautics
Engineering, School of Aerospace Engineering,
Tsinghua University
Beijing 100084 (P.R. China)

Prof. Yonggang Huang
Departments of Civil and Environmental Engineering, Mechanical Engineering, and Materials
Science and Engineering
Northwestern University
Evanston, Illinois 60208 (USA)

†These authors contributed equally to this work.

Keywords: Microelectromechanical systems, 3D microstructures, vibrational modes,
Compressive Buckling

Abstract

Microelectromechanical systems remain an area of significant interest in fundamental and applied research due to their wide ranging applications. Most device designs, however, are largely two-dimensional and constrained to only a few simple geometries. Achieving tunable resonant frequencies or broad operational bandwidths requires complex components and/or fabrication processes. The work presented here reports unusual classes of three-dimensional (3D) micromechanical systems in the form of vibratory platforms assembled by controlled compressive buckling. Such 3D structures can be fabricated across a broad range of length scales and from various materials, including soft polymers, monocrystalline silicon, and their composites, resulting in a wide scope of achievable resonant frequencies and mechanical behaviors. Platforms designed with multistable mechanical responses and vibrationally decoupled constituent elements offer improved bandwidth and frequency tunability. Furthermore, the resonant frequencies can be controlled through deformations of an underlying elastomeric substrate. Systematic experimental and computational studies include structures with diverse geometries, ranging from tables, cages, rings, ring-crosses, ring-disks, two-floor ribbons, flowers, umbrellas, triple-cantilever platforms, and asymmetric circular helices, to multilayer constructions. These ideas form the foundations for engineering designs that complement those supported by conventional, microelectromechanical systems, with capabilities that could be useful in systems for biosensing, energy harvesting and others.

1. Introduction

Microelectromechanical systems (MEMS) exploit structural vibrations for precision mass sensing,^[1-3] microscale rheology,^[4-7] measurement of cell mechanics,^[8-12] and energy harvesting^[13-15] and other important purposes. Current MEMS devices are limited to only a few, largely two-dimensional (2D) geometries such as cantilevered beams,^[16-18] doubly clamped bridges,^[19] stressed wires,^[20] and other constructs based on flat membranes and plates.^[7, 21] These devices also, by consequence, operate in a largely simple, 2D manner, thereby limiting their utility when full, three-dimensional (3D) motions are required. For example, biological cells^[22-25] and tissues^[26-29] have anisotropic mechanical properties. Investigating the mechanical properties of these materials demands devices with capabilities for operation in 3D space. In addition, ambient vibrations are essentially three-dimensional, and hence conventional 2D MEMS devices for kinetic energy harvesting applications have disadvantages. Recent advances in MEMS technologies include the development of devices with resonant frequencies that can be tuned to compensate for frequency shifts associated with changes in the operating environment^[20, 30-32] and that can be continuously adapted for time-varying ambient vibrations, both of which improve the efficiency for energy harvesting. Common methods for tuning the frequency include changing the associated mass and/or tuning the effective stiffness of the resonator by applying stresses through piezoelectric effects, thermal expansion or electrostatic forces.^[20, 30-32] These approaches require, however, integration of additional components and materials, and, therefore, significantly complicate the fabrication process. 3D structures formed via origami,^[33, 34] buckling,^[35-38] and 3D printing^[39] have attracted significant attentions due to their wide range of applications such as microphysiological systems,^[39] cell studies,^[40, 41] bio-mimic actuators,^[42, 43] and the control of wave propagation.^[44, 45] However, their applications in MEMS resonators and energy harvesters remain to be fully explored.

This paper presents a systematic set of experimental and theoretical studies of a broad set of 3D vibrational structures with diverse geometries, assembled by controlled compressive buckling from advanced materials including soft polymers, brittle silicon, and their composites, with potential use as 3D MEMS resonators and kinetic energy harvesters. These platforms offer resonant frequencies that can be tuned by varying the in- and out-of-plane sizes and compositions of the structures or by inducing deformations in the underlying elastomeric substrates. Multistable structures provide routes to increase the bandwidth and tunability. Demonstrations include a broad set of 3D architectures ranging from tables, cages, rings, ring-disks, ring-crosses, flowers, umbrellas, membrane-cantilever hybrid structures, asymmetric circular helices, to multilayer cage structures.

2. Results and Discussion

Cage and table structures serve as examples to demonstrate the essential physics that underpins the dependence of resonant vibrational frequencies on compressive strains applied on the structures via deformations of the substrate (**Figure 1**). Fabrication follows previously reported approaches in deterministic mechanical assembly.^[46-49] Specifically, a set of microfabrication processing steps first produces a collection of 2D precursor structures. Transfer onto a prestretched elastomeric substrate after treating the contacting surfaces to define a collection of sites for strong mechanical bonding prepares the system for geometrical transformation into a 3D structure. Here, relaxing the stretch in the substrate imposes compressive forces on the 2D precursors at the bonding sites, and leads to delamination and consequent out-of-plane translational and rotational motions of the non-bonded regions. The Experimental Section describes the details. Here, the resulting 3D structures serve as vibrational platforms on elastomeric substrates. Controlling the deformation of the latter offers a means for adjusting the 3D geometries and, by consequence, the resonant frequencies.

Figure 1a,b presents scanning electron microscope (SEM) images and results of 3D finite element analyses (FEA) for the cage and table structures compressed at 20%, 30%, and 40% biaxial strains (denoted as ϵ_{comp}). The values of ϵ_{comp} correspond to magnitude of strain released from the substrate initially in its prestretched state. Each structure consists of a patterned layer of a photodefinable polymer (SU8, MicroChem) with thicknesses of 10 μm , and widths of 200 μm (table) and 50 μm (cage) for the support features. (**Figure S1** (Supporting Information) presents detailed geometries for the 2D precursors in both cases. Figure 1a,b shows that, as the compressive strains increase, the in-plane sizes of the cage and table structures decrease and heights increase, as expected. The resulting geometries, in all cases, show good agreement with the FEA. **Figure 1c,d** illustrates two representative vibrational modes, left-right and back-front modes, obtained by FEA. Here, the images in green and grey correspond to the shapes of the 3D structure at two utmost phases (denoted by phases 0° and 180°) during harmonic motions. Due to the thin geometries of the features, cooperative deformations of different components occur mainly by bending and twisting.

A system that captures the time dependence of laser light scattered from the vibrating structures yields frequencies and amplitudes associated with the motions. **Figure 1e,f** presents the measured amplitude-frequency responses of the cage structures in Figure 1a,b for the left-right and back-front modes. Although the amplitudes depend linearly on the intensity of the scattered laser light for a given experimental configuration, comparisons between different structures are difficult due to variations in geometry and baseline values of scattered light. As a result, Figure 1e,f presents the amplitudes normalized by the value at resonance, to facilitate comparisons between the experimental results. The Experimental Section describes the details of the measurement system and method. The results in Figure 1e,f show that resonant

frequencies decrease as the compressive strains increase, confirming the tunability by substrate deformation mentioned previously. As a comparison, **Figure 1g** shows corresponding FEA results. Due to the four-fold rotational symmetry of these two structures, the left-right and the back-front modes have the same amplitude-frequency responses in FEA. **Figure 1h** summarizes the values of resonant frequencies obtained from experiments and FEA. For the left-right mode, the measured resonant frequency reduces from 6.45 kHz and 5.85 kHz to 5 kHz when the compressive strain increases from 20% and 30% to 40%, respectively. The resonant frequencies for the back-front mode are 6.4 kHz, 5.95 kHz, and 5 kHz for 20%, 30%, and 40% biaxial compressive strains, respectively. The FEA results confirm the monotonically decreasing relation between resonant frequencies and compressive strains. **Figure S1** (Supporting Information) presents the vibrational modes and resonant frequencies of the up-down mode corresponding to 20%, 30%, and 40% biaxial compressive strains. The dependence of the resonant frequency on the compressive strain can be mainly attributed to changes in the shapes of the 3D structures. In general, the resonant frequency (f) relates to the effective stiffness (K) and effective mass (M) of a vibrational system by $f = \sqrt{K/M}$, where K and M are dependent on the shape, material properties, and the vibrational mode of the 3D structure. The shapes of the 3D structures change significantly with compressive strain, thereby inducing changes in the resonant frequency, but without significantly affecting the nature of the vibrational mode.

Figure 1i,j shows experimental and FEA resonant frequencies of table structures at 20%, 30%, and 40% biaxial compressive strains and three length scales (denoted as Scales 1, 2, and 3). The in-plane size and thickness of the 2D precursor for Scale 3 are 800 μm and 4 μm , respectively. The in-plane sizes of Scales 1 and 2 structures are 3 and 2 times of the Scale 3 structures, and their thicknesses are 10 μm and 7 μm , respectively. **Figure S1b** (Supporting

Information) shows SEM images of the three structures at the same strain, demonstrating their nearly identical overall shapes. At each scale, the resonant frequencies decrease with increasing compressive strains. At each compressive strain, the resonant frequencies increase as the dimensions decrease. The FEA results show good quantitative agreement with experimental measurements. The conclusion is that a wide range of resonant frequencies can be achieved by varying the compressive strains or scaling the dimensions without changing shape.

The resonant frequencies also depend on material composition and structural dimensions (**Figure 2**). Cage structures serve as examples to demonstrate sensitivity to composition. **Figure 2a** presents SEM images and FEA results of three representative cage structures made of a single layer of SU8, a bilayer of SU8 and monocrystalline Si, and a single layer of monocrystalline Si (left to right). **Figure 2c** shows two representative vibrational modes, left-right and up-down modes, obtained by FEA. **Figure 2e,f** presents the measured amplitude-frequency responses of these modes. Results in Figure 2e,f include three cage structures (denoted as Scale 1 in **Figure 2e,f**) constructed of SU8 (10 μm), SU8 (8.5 μm) / silicon (1.5 μm), and SU8 (5 μm) / Si (1.5 μm), and two cage structures whose in-plane sizes are a factor of two smaller than those at Scale 1. Because the modulus (130 GPa) of Si is much larger than that (4.02 GPa) of SU8, the 3D cage structure made of SU8 (8.5 μm) / Si (1.5 μm) has a much higher resonant frequency than that of the SU8 (10 μm), even though both the lateral sizes and the total thicknesses are the same. The resonant frequencies of the smaller cage structures (Scale 2, i.e. half the size of Scale 1 cages) are higher than all three of the Scale 1 cage structures. The 3D cage of Si (1.5 μm) has higher resonant frequencies than those of the SU8 (5 μm), because the effect of the modulus overcomes that of the thickness in this case.

A scaling law provides quantitative understanding of the effect of material and geometrical parameters on the resonant frequency. For a vibrational mode dominated by bending, the effective stiffness (K) of the 3D structure is proportional to $\hat{E}h^3/L^2$, where \hat{E} is the equivalent modulus, h the total thickness and L the lateral size; the effective mass (M) is proportional to $\hat{\rho}hL^2$, with $\hat{\rho}$ being the equivalent density. Therefore, the resonant frequency can be written as

$$f = \alpha (K / M)^{1/2} = \alpha \hat{E}^{1/2} \hat{\rho}^{-1/2} h L^{-2}, \quad (1)$$

where α is a dimensionless factor that depends on the shape of 3D structure and the vibrational mode and can be determined from FEA. For a bilayer composite of SU8 and Si, the expressions for \hat{E} and $\hat{\rho}$ are

$$\hat{E} = \frac{E_{\text{SU8}}^2 h_{\text{SU8}}^4 + 4E_{\text{SU8}} E_{\text{Si}} h_{\text{SU8}}^3 h_{\text{Si}} + 6E_{\text{SU8}} E_{\text{Si}} h_{\text{SU8}}^2 h_{\text{Si}}^2 + 4E_{\text{SU8}} E_{\text{Si}} h_{\text{SU8}} h_{\text{Si}}^3 + E_{\text{Si}}^2 h_{\text{Si}}^4}{(E_{\text{SU8}} h_{\text{SU8}} + E_{\text{Si}} h_{\text{Si}})(h_{\text{SU8}} + h_{\text{Si}})^3}, \text{ and} \quad (2)$$

$$\hat{\rho} = \frac{\rho_{\text{SU8}} h_{\text{SU8}} + \rho_{\text{Si}} h_{\text{Si}}}{h_{\text{SU8}} + h_{\text{Si}}}, \quad (3)$$

where $E_{\text{SU8}}, E_{\text{Si}}, \rho_{\text{SU8}}, \rho_{\text{Si}}, h_{\text{SU8}}$, and h_{Si} are the Young's modulus, density and thickness of SU8 and Si, respectively. This scaling law agrees well with the experiment results in **Figure 2g and h** and the FEA results in **Figure S3** (Supporting Information) for a wide range of parameters.

Studies of three structures (ring, ring-cross, and ring-disk structure) demonstrate the relationship between the resonant frequencies and the length scales (**Figure 2b**). **Figure 2b** presents SEM images and FEA results. The vibrational direction lies along the two bonding sites, and **Figure 2d** presents their vibrational modes. **Figure 2i** shows the resonant frequencies of the ring and table structures, plotted against their lateral sizes normalized by the largest scale. The results illustrate that the resonant frequencies increase as the sizes

decrease. This scaling is consistent with that observed in ring-cross and ring-disk structures at two length scales (**Figure 2j**). The relationship in Eq. (1) also applies to 3D structures made of a single material, where the equivalent modulus \hat{E} and density $\hat{\rho}$ simply become the modulus E and density ρ of this material. The scaling agrees well with FEA results for more than 10 different 3D structures including the four structures studied here (table, ring, ring-cross, and ring-disk structure), as shown by **Figures S4** and **S5** (Supporting Information), as well as the experimental results in **Figure 2k,l**.

Two-floor structures demonstrate that broadband amplitude-frequency behavior can be achieved by mechanically multistable 3D vibrational platforms (**Figure 3**). **Figure 3a** shows a top-view SEM image and FEA results of three structures in SU8 (10 μm), fabricated using the same process from identical precursors formed at the same time, that are in three stable states. The ribbons on the second floor exhibit three different stable states: 0 downward ribbon (state 1), 1 downward ribbon (state 2), and 2 downward ribbons (state 3). Each of the three structures corresponds to a local minimum in the total strain energy. FEA indicates that a small perturbing force applied at the initial stage of the buckling process can cause the structure to transform from one state to another. By contrast, this perturbing force must be large if applied after 3D assembly. **Figure 3b** illustrates left-right and up-down resonant modes of the three states, and **Figure 3c,d** presents the measured amplitude-frequency responses. Resonant frequencies of the left-right mode vary significantly among these cases. State 1 (0 downward ribbon) has the highest resonant frequency at 15.4 kHz. The resonant frequencies of states 2 and 3 are 12.95 kHz and 11.5 kHz, respectively. Therefore, the resonant frequencies of the left-right mode decrease as the number of downward ribbons increases. The up-down mode follows the same trend, although with a comparatively small magnitude. The resonant frequencies of the up-down mode are 18.8 kHz, 18.65 kHz, and 17.5

kHz, respectively, for states 1, 2, and 3. **Figure 3e** summarizes the measured resonant frequencies and the values obtained by FEA, with good agreement (discrepancies less than 7%).

The resonant frequencies of each of these states can be continuously tuned by compressive strain. This capability can be combined with the strategies in state transfer to achieve broadband tunability of resonant frequency in the two-floor multistable structure. A process of design optimization of the shape in 2D precursor illustrates the opportunities. Here, the resonant frequency (f) is first normalized by $\alpha = fL^2\rho^{1/2}E^{-1/2}h^{-1}$ to exclude the influence of the lateral size (L), the thickness (h) and the material properties (E, ρ). Fixing the size, the widths of the ribbon in the x - direction (w_x) and the y - direction (w_y) serve as the two variables to be optimized, as shown in the inset of **Figure 3f**. The target is to maximize the ratio ($\alpha_{\max}/\alpha_{\min}$), in which α_{\max} and α_{\min} represent the maximum and minimum resonant frequencies of the three buckling states as the compressive strain varies in the range of 10% to 50%. A design constraint is that the resonant frequency should be tunable in a continuous manner from the minimum to the maximum value without any gap. Only the first order mode, namely the left-right mode, is considered. The ratio $\alpha_{\max}/\alpha_{\min}$ appears as a function of L/w_x and w_y/w_x in **Figure 3f**. The optimal design reaches a ratio of $\alpha_{\max}/\alpha_{\min} = 2.25$, and in this case, the normalized resonant frequency α can be continually tuned from 0.59 to 1.31 as shown by **Figure 3g**. Note that only two buckling states (1 and 2) are needed to achieve the tunable resonant frequency band, as the other state (i.e., state 3) does not provide any additional broadening.

A set of complex 3D structures illustrates the diversity of vibrational behavior that can be realized (**Figure 4**). **Figure 4a** shows SEM images and FEA results of a six-fold rotationally

symmetric flower structure (SU8, 10 μm in thickness) and its amplitude-frequency response for the left-right mode. The first resonance corresponds to the vibration of the petal tip. **Figure 4b** presents an eight-fold rotationally symmetric umbrella structure (SU8, 10 μm in thickness). Similar to the flower structure, amplitude-frequency response of the left-right mode exhibits a single peak that corresponds to a global resonance of the structure. Asymmetric geometries are also possible. **Figure 4c** illustrates a triple-cantilever structure (SU8, 10 μm in thickness) that has cantilever beams with different lengths connected to a triangular membrane. The beam “B1” is the longest, and “B3” is the shortest. Therefore, the resonant frequency of B1 is lowest, and B3 is highest. The resonant frequency of the membrane is higher than that of the beams. **Figure S6c** (Supporting Information) shows its vibrational modes. The resonance of the beam is localized and largely decoupled from deformations of the membrane. By contrast, the resonance of the membrane leads to global vibration of the entire structure. This example illustrates the ability to decouple local and global resonances in complex 3D vibrational platforms. **Figure 4d** presents an asymmetric circular helix (SU8, 10 μm in thickness) that consists of eight ribbons with different lengths. **Figure 4d** also includes the frequency responses of four ribbons with different lengths. The eighth ribbon is the shortest, and hence its resonant frequency is highest. Various resonances are therefore readily achievable in a single structure. **Figure 4e** highlights a multilayer cage structure and its amplitude-frequency responses. The lateral size of the lower layer (SU8, 7 μm in thickness) is 50% of the upper layer (SU8, 10 μm in thickness), resulting in a higher resonant frequency. **Figure 4f** shows comparisons between measured resonant frequencies and FEA results, with good agreement (discrepancies less than 7% for all structures).

3. Conclusion

In summary, this paper presents a systematic study of vibrational modes in 3D structures assembled by compressive buckling. These systems provide high levels of versatility in

design of vibrational responses, through (1) structural complexity and dimensional scaling enabled by the assembly process, (2) diversity in materials selections, in single or multicomponent layouts, (3) reversible geometrical tunability enabled by the mechanical elasticity of the substrate. Multistable mechanics and vibrational decoupling of multiple resonant modes represent some consequent strategies for broadband operation, of utility in mechanical resonators, kinetic energy harvesters and other applications. Rotationally symmetric structures, asymmetric networks, and nested, multilayer layouts can be adapted for various additional mechano-vibratory responses. These results suggest that such classes of 3D structures offer potentially important design options that lie outside of the scope of possibilities supported by traditional MEMS technologies.

From a design perspective, the results presented in this paper provide several important considerations and options. (1) Decreasing the lateral dimensions and increasing the stiffnesses of 3D microstructures that consist main ribbons increases their resonant frequencies and therefore improves their detection limits when used for mass sensing. (2) Reversible geometrical deformations of 3D microstructures alter their resonant frequencies in well-defined ways, of relevance for devices that require tunable response. (3) Selection of constituent materials provides a route to meet requirements for operating frequencies in devices that involve a fixed, or a narrow range of in-plane dimensions. (4) Multistable 3D microstructures offer alternative options for broadband frequency operation, of importance for use in mechanical energy harvesters. (5) Multilayer and asymmetric 3D microstructures can serve as ideal platforms for devices that require multiple separated resonant frequencies and modes.

4. Experimental Section

Fabrication of 3D structures in SU8, Si, and SU8/Si followed previously reported procedures.^[46-49] **Figure S7** (Supporting Information) presents a schematic illustration of the fabrication procedures. Preparation of SU8 3D structures began with spin-casting SU8 on a silicon wafer with a layer of thermally grown silicon dioxide (SiO₂, 800 nm in thickness), followed by a photolithographic procedure to produce 2D precursors. Immersing the wafer in buffered oxide etch (BOE) removed the exposed SiO₂ and slightly etched the SiO₂ underneath the precursors. Spin-casting and photolithography defined a layer of photoresist (AZ5214E, MicroChemicals) to cover the precursors except their bonding sites. The AZ5214E served as a sacrificial layer to facilitate transformation of precursors into 3D structures, described below. Immersing the wafer in hydrofluoric acid (HF) fully removed the SiO₂ and finished fabrication of SU8 precursors. Transferring the precursors onto a PDMS stamp and then to a sheet of water soluble tape (polyvinyl alcohol, PVA) prepared samples for compressive buckling on an elastomeric substrate. Exposing a prestretched sheet of silicone elastomer (Dragon Skin, Smooth-on) and the precursors on the PVA tape to UV induced ozone activated hydroxyl termination to facilitate bonding between the precursors and elastomeric substrate. Attaching the PVA tape on the substrate and baking them in an oven at 70 °C for 9 minutes yielded strong bonding. Immersing in hot water and then in acetone removed the PVA tape and the AZ5214E sacrificial layer. Releasing the stretched substrate geometrically transformed the 2D precursors into 3D structures. Preparation of 3D structures of Si began with photolithographic patterning of etching masks (AZ5214E) on a silicon-on insulator (SOI) wafer. Reactive ion etching (RIE) of the exposed regions of the top silicon layer (1.5 μm in thickness) defined the geometry of the 2D Si precursors. Immersion in Nanostrip at 100 °C for 10 minutes removed the AZ5214E. The remaining steps were identical to those for the SU8 structures. Preparation of SU8/Si structures combined the steps described above. In particular, the process began with patterning the Si layer of a SOI wafer, followed by spin-casting an

adhesive layer (OmniCoat, MicroChem) to improve adhesion between Si and SU8. The remaining steps were identical to those for the SU8 structures.

A 3D-printed testing stage and piezoelectric actuators excited vibrations of 3D structures under test (**Figure S8** (Supporting Information)). **Figure S8a** shows an optical image of the stage and actuators. The latter consisted of a central platform, translational arms, slots for housing actuators, and a base frame. Two piezoelectric chips (Thorlabs, 75 V Piezoelectric Chips, 2.8 μm in stroke) placed in two slots of the stage served as actuators to excite vibrations of 3D structures. A function generator (Keithley 3390) applied sinusoidal voltage on the actuators, thereby exciting vibrations at desired frequencies. A positive driving voltage created expansion in the actuators and associated applied forces on the translational arms, leading to vibration of the central platform. The elastomeric substrate for the 3D structures under test was attached to the central platform by a layer of double-sided tape. Vibration of the platform led to vibrations in the 3D structure. The testing stage can generate vibrations in X- and Y- directions (parallel to the surface of elastomer substrate). Placing 3D structures on the top surface of an actuator (**Figure S8b**) generated vibrations in the Z-direction (perpendicular to the surface of elastomer substrate).

A laser measurement system served as the apparatus to investigate the dynamic behavior of 3D structures (**Figure S8c** (Supporting Information)). A focusing lens and mirror delivered a focused laser beam onto a targeted region of a 3D structure under test. The 3D structure and supporting stage were mounted on a mechanical stage capable of translation in X-, Y-, and Z- directions and tilt with respect to X- and Y- axes. Light scattered from the 3D structures was reflected by a second mirror, collected by a second lens and directed to a photodetector (Thorlabs, DET110) to allow measurement of the intensity. In each measurement the position of the 3D structure was carefully adjusted to ensure that the laser beam focused on the

structure and the scattered light was collected by the photodetector. A microscope facilitated the focusing and aligning operations. A pinhole shutter placed in front of the photodetector allowed only a fraction of the scattered laser to be collected by the photodetector. Vibrations of the 3D structure created fluctuations in the intensity of scattered laser collected by the photodetector, with the same overall time dependence. A lock-in amplifier (SRS 830, Stanford Research Systems) measured the amplitude of fluctuating photocurrent. This system does not, of course, directly determine the vibrational amplitude. In each case, the setups were adjusted such that the amplitude of the photocurrent responded linearly to the amplitude of driving voltage. In this regime of operation, the amplitude of the fluctuating photocurrent is directly proportional to the vibrational amplitude. The amplitude of the photocurrent measured in this way reached a maximum at the resonant frequency. A Labview program automatically swept the desired range of frequency and recorded data from the lock-in amplifier. At each frequency, the program waited for 4 seconds before recording data, to ensure stable vibration. 64 data points were recorded at each frequency and the increment of frequency was 50 Hz. All the amplitude-frequency curves presented in this paper were the average among the 64 data points at each frequency.

Supporting Information

Supporting Information is available from the Wiley Online Library or from the author.

Acknowledgements

X.N, H.W, and X.Y contributed equally to this work. Y.H. acknowledges the support from the NSF (Grant Nos. DMR-1121262, CMMI-1300846, and 1534120). Y.H. and J.A.R. acknowledge the support from the NSF (Grant No. CMMI-1400169) and the NIH (Grant No. R01EB019337). Y.Z. acknowledges the support from the National Science Foundation of China (Grant No. 11672152). J.A.R. acknowledges the support from the U.S. Department of Energy, Office of Science, Basic Energy Sciences under Award # DEFG02-07ER46471.

Received: ((will be filled in by the editorial staff))

Revised: ((will be filled in by the editorial staff))

Published online: ((will be filled in by the editorial staff))

References

- [1] K. Jensen, K. Kim, A. Zettl, *Nat Nano*, **2008**, 3, 533.
- [2] M. S. Hanay, S. Kelber, A. K. Naik, D. Chi, E. C. Bullard, E. Colinet, L. Duraffourg, M. L. Roukes, *Nat Nano*, **2012**, 7, 602.
- [3] T. P. Burg, M. Godin, S. M. Knudsen, W. Shen, G. Carlson, J. S. Foster, K. Babcock, S. R. Manalis, *Nature*, **2007**, 446, 1066.
- [4] I. Etchart, H. Chen, P. Dryden, J. Jundt, C. Harrison, K. Hsu, F. Marty, B. Mercier, *Sensor Actuat A-Phys*, **2008**, 141, 266.
- [5] N. Belmiloud, I. Dufour, A. Colin, L. Nicu, *Appl. Phys. Lett.*, **2008**, 92, 041907.
- [6] S. Boskovic, J. W. M. Chon, P. Mulvaney, J. E. Sader, *J. Rheol.*, **2002**, 46, 891.
- [7] S. Cerimovic, R. Beigelbeck, H. Antlinger, J. Schalko, B. Jakoby, F. Keplinger, *Microsys. Technol.*, **2012**, 18, 1045.
- [8] C. Moraes, C. A. Simmons, Y. Sun, *CSME Bulletin SCGM*, **2006**, 15.
- [9] K. Park, L. J. Millet, N. Kim, H. Li, X. Jin, G. Popescu, N. R. Aluru, K. J. Hsia, R. Bashir, *Proc. Natl. Acad. Sci.*, **2010**, 107, 20691.
- [10] K. Park, L. Millet, N. Kim, H. Li, K. J. Hsia, N. R. Aluru, R. Bashir, " 2011 16th International Solid-State Sensors, Actuators and Microsystems Conference, 5-9 June 2011, 2011.
- [11] R. Jagannathan, M. T. A. Saif, *J. Micromech. Microeng.*, **2011**, 21, 054002.
- [12] M. Unal, Y. Alapan, H. Jia, A. G. Varga, K. Angelino, M. Aslan, I. Sayin, C. Han, Y. Jiang, Z. Zhang, *Nanobiomedicine*, **2014**, 4: 7173.
- [13] P. Christian, M. Dominic, S. Wolfram, M. Florian, M. Yiannos, *J. Micromech. Microeng.*, **2009**, 19, 094004.

- [14] P. L. Green, E. Papatheou, N. D. Sims, *J. Intell. Mater. Syst. Struct.*, **2013**, 24, 1494.
- [15] G. N. Rameshaiah, J. Pallavi, *Micro Perspectives For Decentralized Energy Supply*, **2015**, 170.
- [16] I. Dufour, A. Maali, Y. Amarouchene, C. Ayela, B. Caillard, A. Darwiche, M. Guirardel, H. Kellay, E. Lemaire, F. Mathieu, C. Pellet, D. Saya, M. Youssry, L. Nicu, A. Colin, *J. Sens*, **2012**, 2012, 9.
- [17] J. Park, S. Jeong, S. J. Kim, J. Park, *Rev. Sci. Instrum.*, **2015**, 86, 015002.
- [18] M. Youssry, N. Belmiloud, B. Caillard, C. Ayela, C. Pellet, I. Dufour, *Sensor Actuat A-Phys*, **2011**, 172, 40.
- [19] B. Jakoby, E. Reichel, F. Lucklum, B. Weiss, C. Riesch, F. Keplinger, R. Beigelbeck, W. Hilber, *Mechanics and Model-Based Control of Smart Materials and Structures*, Springer, Berlin, Germany, 2010.
- [20] H. Cho, M.-F. Yu, A. F. Vakakis, L. A. Bergman, D. M. McFarland, *Nano Letters*, **2010**, 10, 1793.
- [21] S. Lee, C. Chen, V. V. Deshpande, G.-H. Lee, I. Lee, M. Lekas, A. Gondarenko, Y.-J. Yu, K. Shepard, P. Kim, J. Hone, *Appl. Phys. Lett.*, **2013**, 102, 153101.
- [22] H. Takahashi, M. Nakayama, T. Shimizu, M. Yamato, T. Okano, *Biomaterials*, **2011**, 32, 8830.
- [23] K. Lau, H. Tao, H. Liu, J. Wen, K. Sturgeon, N. Sorfazlian, S. Lazic, J. T. A. Burrows, M. D. Wong, D. Li, S. Deimling, B. Ciruna, I. Scott, C. Simmons, R. M. Henkelman, T. Williams, A.-K. Hadjantonakis, R. Fernandez-Gonzalez, Y. Sun, S. Hopyan, *Nat Cell Biol*, **2015**, 17, 569.
- [24] P. Campinho, M. Behrndt, J. Ranft, T. Risler, N. Minc, C.-P. Heisenberg, *Nat Cell Biol*, **2013**, 15, 1405.
- [25] J. Dumais, S. L. Shaw, C. R. Steele, S. R. Long, P. M. Ray, *Int. J. Dev. Biol.*, **2003**, 50, 209.

- [26] Z. W. Chen, P. Joli, Z. Q. Feng, *Comput Methods Biomech Biomed Engin.*, **2015**, 18, 1436.
- [27] J. A. Weiss, B. N. Maker, S. Govindjee, *Comput Method Appl M*, **1996**, 135, 107.
- [28] G. A. Holzapfel, T. C. Gasser, R. W. Ogden, *Journal of elasticity and the physical science of solids*, **2000**, 61, 1.
- [29] D. Balzani, D. Brands, A. Klawonn, O. Rheinbach, J. Schröder, *Arch. Appl. Mech.*, **2010**, 80, 479.
- [30] Z.-E.-A. Imed, Y. Peng, *J. Micromech. Microeng.*, **2009**, 19, 125004.
- [31] J. Olivares, J. Malo, S. González, E. Iborra, I. Izpura, M. Clement, A. Sanz-Hervás, J. L. Sánchez-Rojas, P. Sanz, MEMS, MOEMS, and Micromachining II, 2006.
- [32] W.-M. Zhang, K.-M. Hu, Z.-K. Peng, G. Meng, *Sensors*, **2015**, 15.
- [33] E. T. Filipov, T. Tachi, G. H. Paulino, *Proc. Natl. Acad. Sci. USA*, **2015**, 112, 12321.
- [34] E. T. Filipov, G. H. Paulino, T. Tachi, *Proc. R. Soc. A*, **2016**, 472, 1.
- [35] Y. Chen, Y. Zhu, X. Chen, Y. Liu, *J. Appl. Mech.-Trans. ASME*, **2016**, 83, 041011.
- [36] Y. Chen, Y. Liu, Y. Yan, Y. Zhu and X. Chen, *J. Mech. Phys. Solids*, **2016**, 95, 25.
- [37] P. Froeter, X. Yu, W. Huang, F. Du, M. Li, I. Chun, S. H. Kim, K. J. Hsia, J. A. Rogers, X. Li, *Nanotechnology*, **2013**, 24, 475301.
- [38] W. Huang, S. Koric, Xin Yu, K. J. Hsia, X. Li, *Nano Lett.*, **2014**, 14, 6293.
- [39] J. U. Lind, T. A. Busbee, A. D. Valentine, F. S. Pasqualini, H. Yuan, M. Yadid, S.-J. Park, A. Kotikian, A. P. Nesmith, P. H. Campbell, J. J. Vlassak, J. A. Lewis, K. K. Parker, *Nat. Mater.*, **2016**, in press.
- [40] K. Malachowski, M. Jamal, Q. Jin, B. Polat, C. J. Morris, D. H. Gracias, *Nano Lett.*, **2014**, 14, 4164.
- [41] W. Xi, C. K. Schmidt, S. Sanchez, D. H. Gracias, R. E. Carazo-Salas, S. P. Jackson, O. G. Schmidt, *Nano Lett.*, **2014**, 14, 4197.

- [42] D. Yang, B. Mosadegh, A. Ainla, B. Lee, F. Khashai, Z. Suo, K. Bertoldi, G. M. Whitesides, *Adv. Mater.*, **2015**, 27, 6323.
- [43] D. Yang, M. S. Verma, J.-H. So, B. Mosadegh, C. Keplinger, B. Lee, F. Khashai, E. Lossner, Z. Suo, G. M. Whitesides, *Adv. Mater. Technol.*, **2016**, 1, 1600055.
- [44] S. Babaei, N. Viard, P. Wang, N. X. Fang, K. Bertoldi, *Adv. Mater.*, **2016**, 8, 1631.
- [45] J. R. Raney, N. Nadkarni, C. Daraio, D. M. Kochmann, J. A. Lewis, K. Bertoldi, *Proc. Natl. Acad. Sci. USA*, **2016**, 113, 9722.
- [46] S. Xu, Z. Yan, K.-I. Jang, W. Huang, H. Fu, J. Kim, Z. Wei, M. Flavin, J. McCracken, R. Wang, A. Badea, Y. Liu, D. Xiao, G. Zhou, J. Lee, H. U. Chung, H. Cheng, W. Ren, A. Banks, X. Li, U. Paik, R. G. Nuzzo, Y. Huang, Y. Zhang, J. A. Rogers, *Science*, **2015**, 347, 154.
- [47] Y. Zhang, Z. Yan, K. Nan, D. Xiao, Y. Liu, H. Luan, H. Fu, X. Wang, Q. Yang, J. Wang, W. Ren, H. Si, F. Liu, L. Yang, H. Li, J. Wang, X. Guo, H. Luo, L. Wang, Y. Huang, J. A. Rogers, *Proc. Natl. Acad. Sci.*, **2015**, 112, 11757.
- [48] Z. Yan, F. Zhang, J. Wang, F. Liu, X. Guo, K. Nan, Q. Lin, M. Gao, D. Xiao, Y. Shi, Y. Qiu, H. Luan, J. H. Kim, Y. Wang, H. Luo, M. Han, Y. Huang, Y. Zhang, J. A. Rogers, *Adv. Funct. Mater.*, **2016**, 26, 2629.
- [49] Y. Liu, Z. Yan, Q. Lin, X. Guo, M. Han, K. Nan, K.-C. Hwang, Y. Huang, Y. Zhang, J. A. Rogers, *Adv. Funct. Mater.*, **2016**, 26, 2909.

Figure Captions

Figure 1. Resonant vibrational frequencies of 3D structures and their dependence on compressive strains applied on the structures. a) SEM images and FEA results for 3D cage structures buckled at three strain levels. Scale bar: 1 mm. b) SEM images and FEA results of table structures buckled at three strain levels. Scale bar: 500 μm . c) and d) FEA results for the vibration modes of cage and table structures, respectively, in which the amplitudes are magnified to clearly illustrate the modes. e) and f) Measured amplitude-frequency responses of left-right and back-front vibrational modes, respectively, for cage structures. g) Simulated amplitude-frequency responses of left-right and back-front vibration modes by FEA. h) Comparison between measured and simulated resonant frequencies for cage structures. i) and j) Measured and simulated resonant frequencies of left-right and back-front vibrational modes, respectively, at three strain levels and three dimensional scales for table structures.

Figure 2. Resonant frequencies of 3D structures as a function of material composition and dimensional scale. a) SEM images and FEA results for cage structures comprised of SU8, Si-SU8 composite, and Si. Scale bars: 500 μm . b) SEM images and FEA results for ring, ring-cross, and ring-disk structures. Scale bars: 1 mm. c) and d) FEA images of the vibrational modes, in which the amplitudes are magnified to clearly illustrate the modes. e) and f) Measured amplitude-frequency responses of left-right and back-front vibrational modes, respectively, for various combinations of SU8 and Si thicknesses. The legends represent the thickness ratios between SU8 and Si (unit: μm). g) and h) Experimental results compared with the scaling law for the resonant frequencies for SU8, Si and SU8/Si cage structures. i) Measured resonant frequencies of left-right vibrational modes for table and ring structures at three scales. j) Measured resonant frequencies of left-right vibrational modes for ring-cross and ring-disk structures at two scales. k) Experimental results compared with the scaling law

for the resonant frequencies of table and ring structures. 1) Experimental results compared with the scaling law for the resonant frequencies of ring-cross and ring-disk structures.

Figure 3. Broadband amplitude-frequency responses achieved in 3D structures with multistable mechanics. a) SEM images and FEA results of three stable states of two-floor 3D structures. Scale bar: 500 μm . b) FEA images of vibrational modes, green: phase 0° , grey: phase 180° , in which the amplitudes are magnified to clearly illustrate the modes. c) and d) Measured amplitude-frequency responses of left-right and up-down vibrational modes, respectively. e) Comparison between measured resonant frequencies and simulations. f) Optimization of the operating frequency bandwidth by designing the geometries of the precursor. g) Simulated variations in the normalized resonant frequency as a function of compressive strain for an optimized structure. The normalized resonant frequency can be continuously tuned from 0.59 to 1.31 by changing the compressive strain and shifting the buckled state.

Figure 4. Single-peak and broadband amplitude-frequency responses achieved by structures with diverse 3D geometries. a) SEM images and FEA results for a flower structure (scale bar: 1 mm) and measured amplitude-frequency response for left-right mode. b) SEM images and FEA results of an umbrella structure (scale bar: 1 mm) and measured amplitude-frequency response for the left-right mode. c) SEM images and FEA results of a triple-cantilever structure (scale bar: 2 mm) and measured amplitude-frequency responses of the three beams and central membrane for the left-right mode. d) SEM images and FEA results of a circular helix structure (scale bar: 500 μm) and measured amplitude-frequency responses of the four ribbons with different lengths for the left-right mode. e) SEM images and FEA results of a two-layer cage structure (scale bar: 1 mm) and measured amplitude-

frequency responses of the upper and lower floor for the left-right mode. f) Comparison between measured resonant frequencies and simulations.

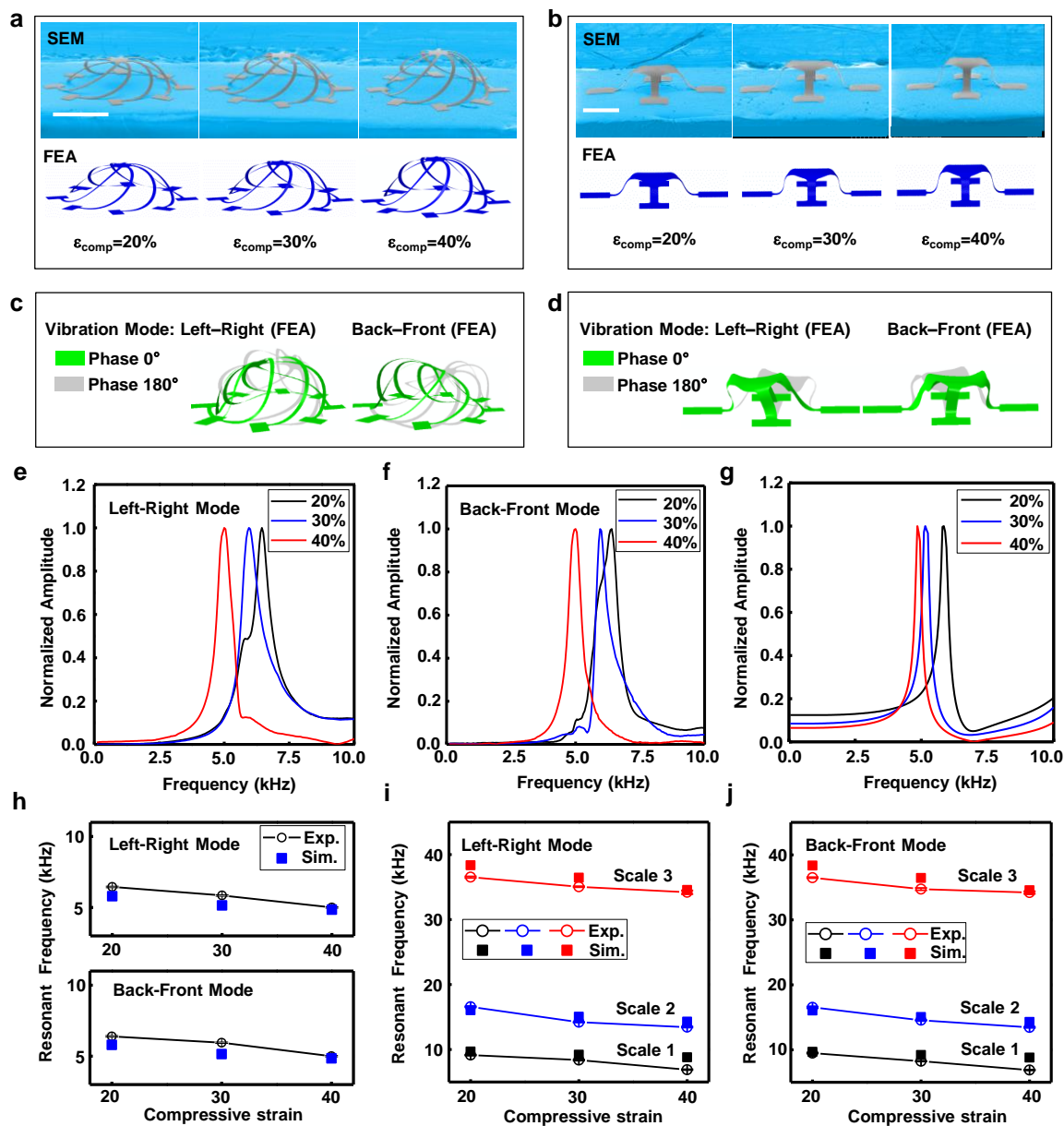


Figure 1

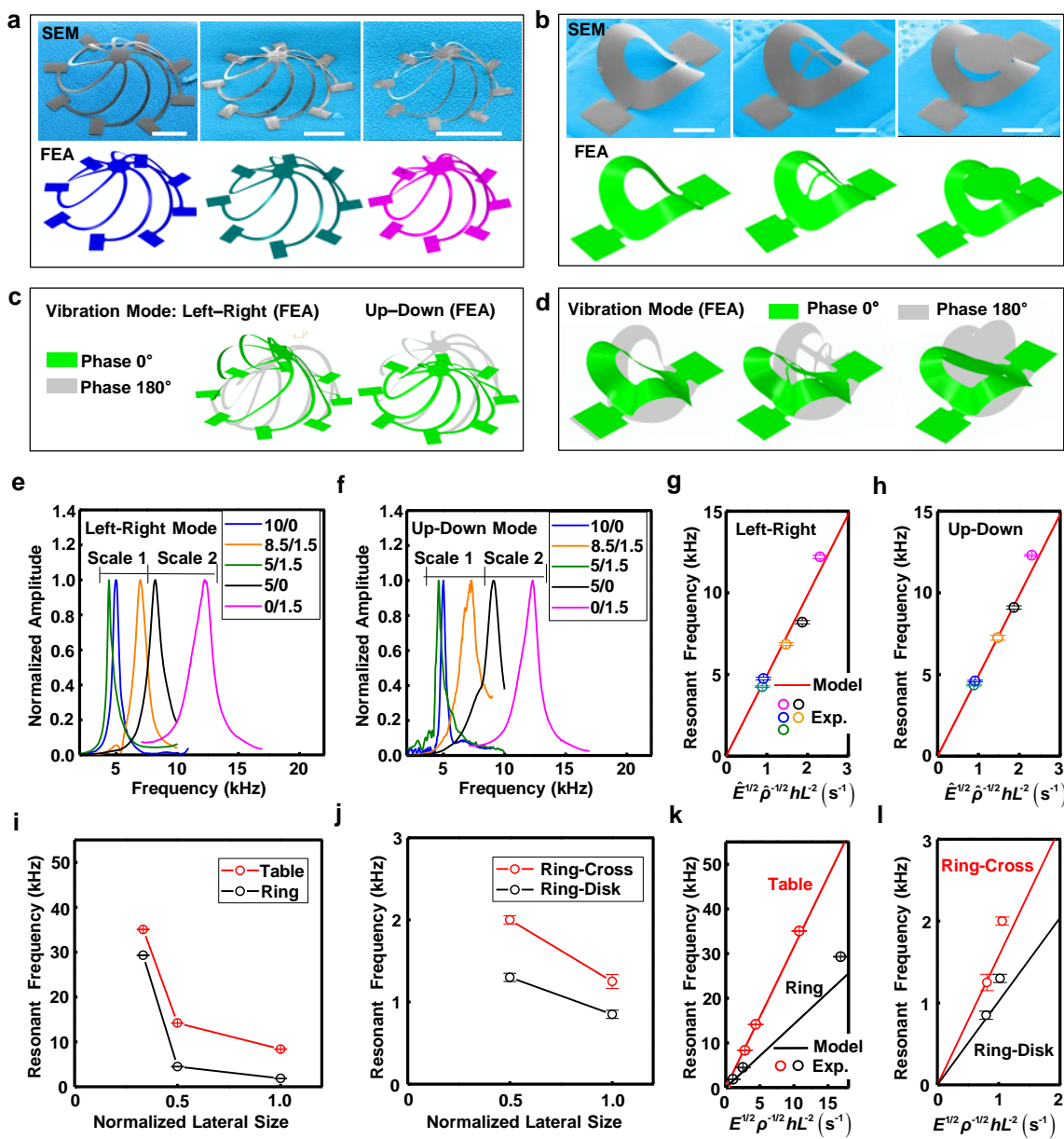


Figure 2

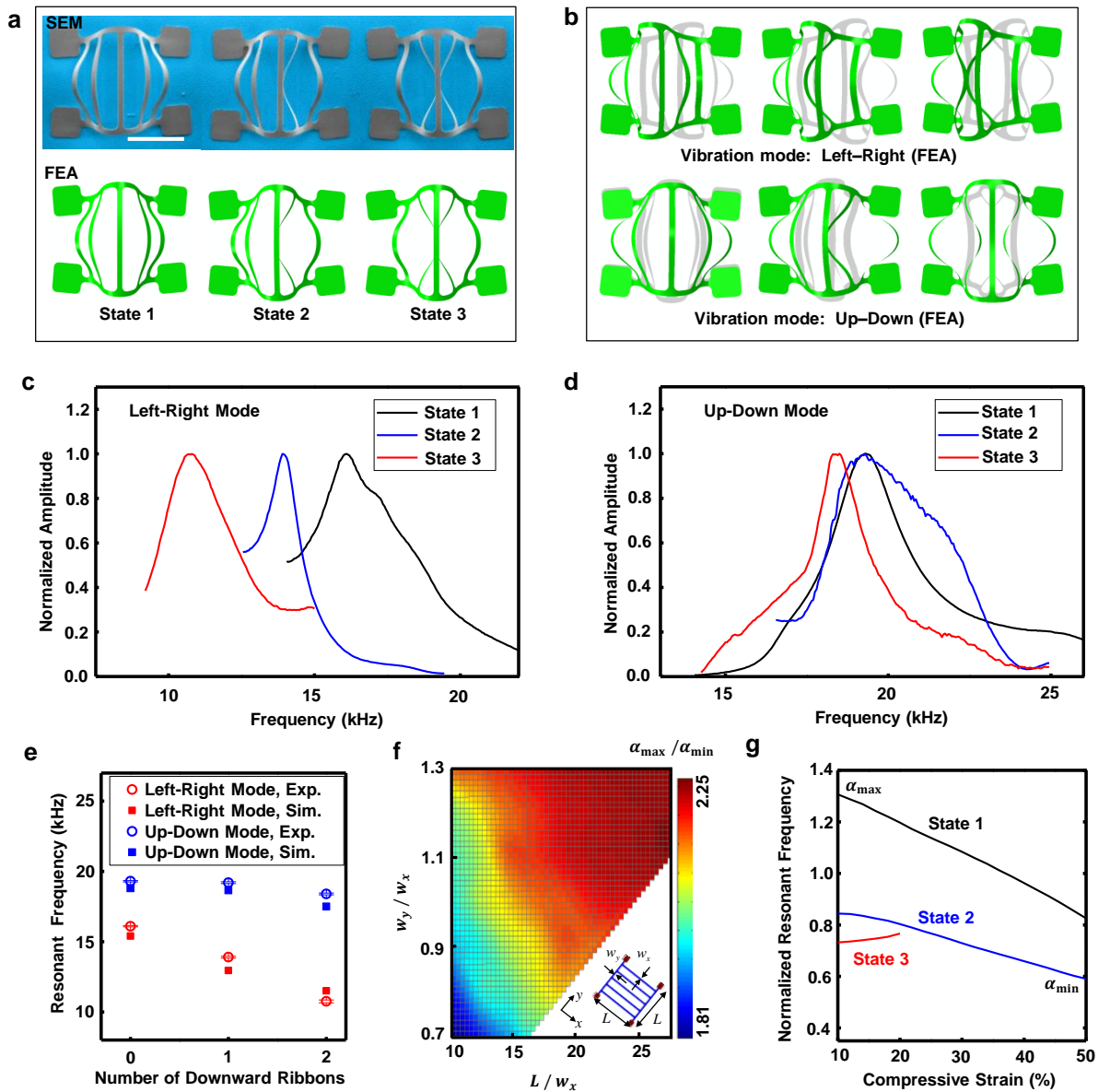


Figure 3

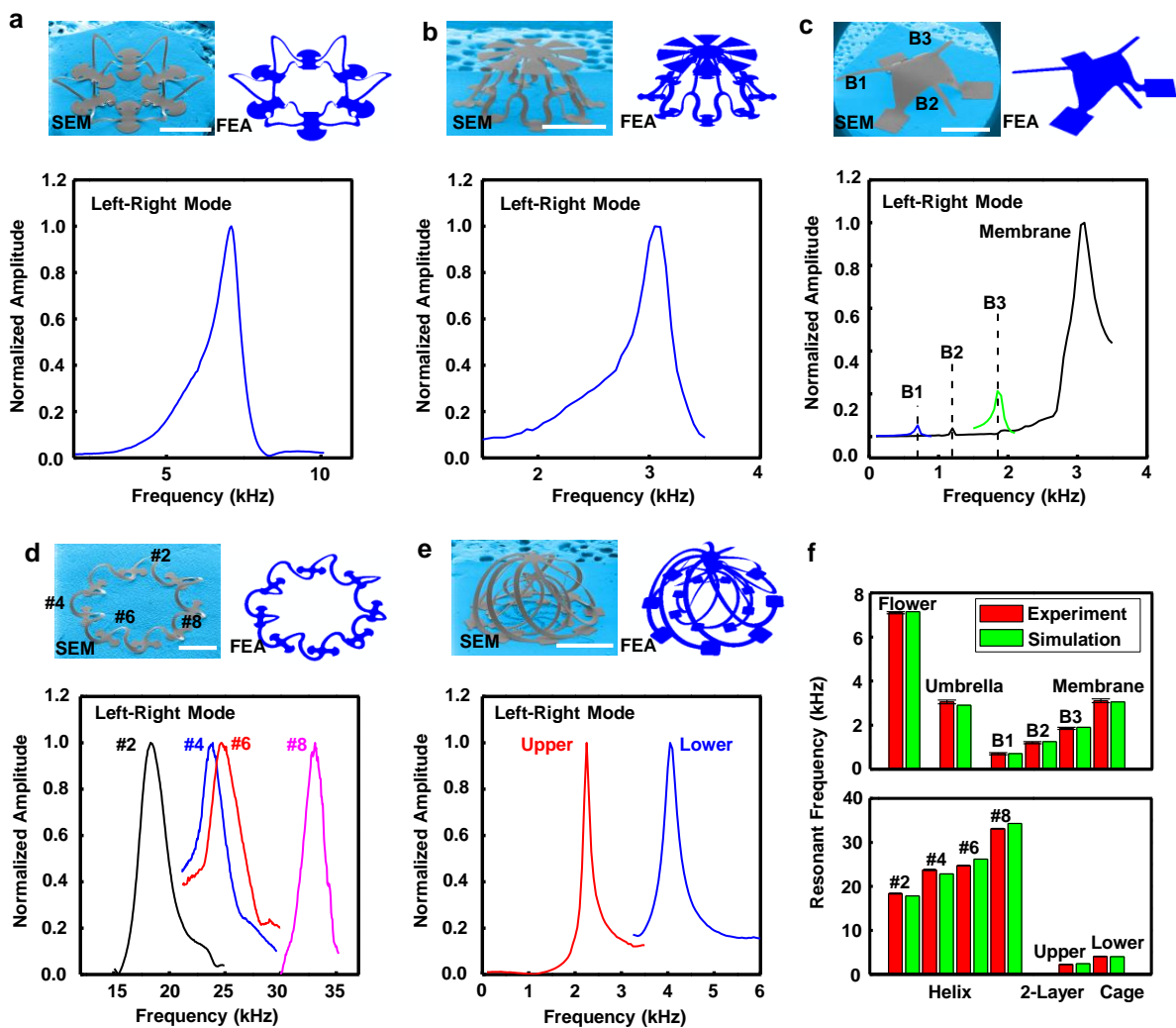


Figure 4

The table of contents entry

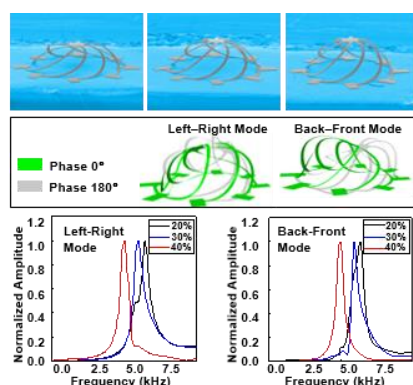
The dynamical behavior of three-dimensional structures assembled by compressive buckling from advanced materials is presented. The results include a broad set of three-dimensional geometries with unique mechanical features, such as tunable resonant frequencies and multistable states. The results provide important design options for MEMS resonators and kinetic energy harvesters.

Keywords: Microelectromechanical systems, 3D microstructures, vibrational modes, Compressive Buckling

Authors: Xin Ning[†], Heling Wang[†], Xinge Yu[†], Julio A. N. T. Soares, Zheng Yan, Kewang Nan, Gabriel Velarde, Yeguang Xue, Rujie Sun, Qiyi Dong, Haiwen Luan, Chan Mi Lee, Aditya Chempakasseril, Mengdi Han, Yiqi Wang, Luming Li, Yonggang Huang, Yihui Zhang*, John Rogers*

Title: Three-Dimensional Tunable, Multiscale, Multistable, and Diverse Vibrational Platforms Assembled by Compressive Buckling

ToC figure ((Please choose one size: 55 mm broad \times 50 mm high **or** 110 mm broad \times 20 mm high. Please do not use any other dimensions))



Supporting Information

Three-Dimensional Multiscale, Multistable, and Geometrically Diverse Microstructures with Tunable Vibrational Dynamics Assembled by Compressive Buckling

Xin Ning[†], Heling Wang[†], Xinge Yu[†], Julio A. N. T. Soares, Zheng Yan, Kewang Nan, Gabriel Velarde, Yeguang Xue, Rujie Sun, Qiyi Dong, Haiwen Luan, Chan Mi Lee, Aditya Chempakasseril, Mengdi Han, Yiqi Wang, Luming Li, Yonggang Huang, Yihui Zhang, John Rogers**

[*] Prof. John A. Rogers, Corresponding-Author
Department of Materials Science and Engineering, Biomedical Engineering, Neurological Surgery, Chemistry, Mechanical Engineering, Electrical Engineering and Computer Science
Simpson Querrey Institute and Feinberg Medical School
Center for Bio-Integrated Electronics
Northwestern University
Evanston, Illinois 60208 (USA)
E-mail: jrogers@northwestern.edu

[*] Prof. Yihui Zhang, Corresponding-Author
Center for Mechanics and Materials, AML, Department of Engineering Mechanics,
Tsinghua University
Beijing 100084 (P.R. China)
E-mail: yihui Zhang@tsinghua.edu.cn

Dr. Xin Ning, Dr. Xinge Yu, Dr. Julio A.N.T. Soares, Dr. Zheng Yan, Mr. Kewang Nan, Mr. Gabriel Velarde, Mr. Yiqi Wang
Department of Materials Science and Engineering
Frederick Seitz Materials Research Laboratory
University of Illinois at Urbana-Champaign
Urbana, Illinois 61801 (USA)

Mr. Rujie Sun
Advanced Composites Centre for Innovation and Science,
University of Bristol
Bristol, BS8 1TR (UK)

Dr. Heling Wang, Mr. Yeguang Xue, Mr. Haiwen Luan
Departments of Civil and Environmental Engineering, and Mechanical Engineering
Northwestern University
Evanston, Illinois 60208 (USA)

Mr. Qiyi Dong
Department of Industrial and Enterprise Systems Engineering
University of Illinois at Urbana-Champaign
Urbana, Illinois 61801 (USA)

Ms. Chan Mi Lee
Collage of Liberal Arts and Sciences
University of Illinois at Urbana-Champaign
Urbana, Illinois 61801 (USA)

Mr. Aditya Chempakasseril
Department of Chemical and Biomolecular Engineering
University of Illinois at Urbana-Champaign
Urbana, Illinois 61801 (USA)

Mr. Mengdi Han
National Key Laboratory of Science and Technology on Micro/Nano Fabrication,
Peking University, Beijing 100871 (P.R. China)

Prof. Luming Li
Man-machine-Environment Engineering Institute, Department of Aeronautics & Astronautics
Engineering, School of Aerospace Engineering,
Tsinghua University
Beijing 100084 (P.R. China)

Prof. Yonggang Huang
Departments of Civil and Environmental Engineering, Mechanical Engineering, and Materials
Science and Engineering
Northwestern University
Evanston, Illinois 60208 (USA)

†These authors contributed equally to this work.

Keywords: Microelectromechanical systems, 3D microstructures, vibrational modes,
Compressive Buckling

1. Finite Element Analysis

FEA obtained the shape of the 3D structure during mechanically-guided assembly, the vibrational mode of the buckled 3D structure, and its resonant frequency. A postbuckling analysis on a 2D precursor under compression provided the shape of the 3D structure upon release of the prestretched elastomer substrate. For the two-floor structure that has multistable states, a small disturbing force introduced at the initial stage of compression guided the structure to evolve towards a certain state. For other structures, an initial geometric imperfection obtained by a previous linear buckling analysis facilitated the buckling process and achieve desired first-order buckling mode. The FEA used eight-node 3D solid elements for the substrate and four-node 3D shell elements for precursors. Refined meshes for both the substrate and the precursor guaranteed the accuracy of analyses. Steady-state dynamic analyses provided vibrational modes and resonant frequencies. The amplitude-frequency response curve was obtained by using an interval of 20 Hz in the frequency sweeping, from which the resonant frequency (corresponding to the peak of the curve) can be determined. The FEA models used stiffness proportional damping factors $\beta_{\text{substrate}} = 10^{-4}$ and $\beta_{\text{precursor}} = 10^{-6}$ to include the dissipations of substrates and precursors, respectively. The density (ρ), Young's modulus (E) and Poisson's ratio (ν) were $\rho_{\text{SU8}} = 1219 \text{ kg/m}^3$, $E_{\text{SU8}} = 4.02 \text{ GPa}$ and $\nu_{\text{SU8}} = 0.22$ for SU8; $\rho_{\text{Si}} = 2328 \text{ kg/m}^3$, $E_{\text{Si}} = 130 \text{ GPa}$ and $\nu_{\text{Si}} = 0.27$ for silicon; $\rho_{\text{substrate}} = 1070 \text{ kg/m}^3$, $E_{\text{substrate}} = 166 \text{ kPa}$ and $\nu_{\text{substrate}} = 0.49$ for substrate.

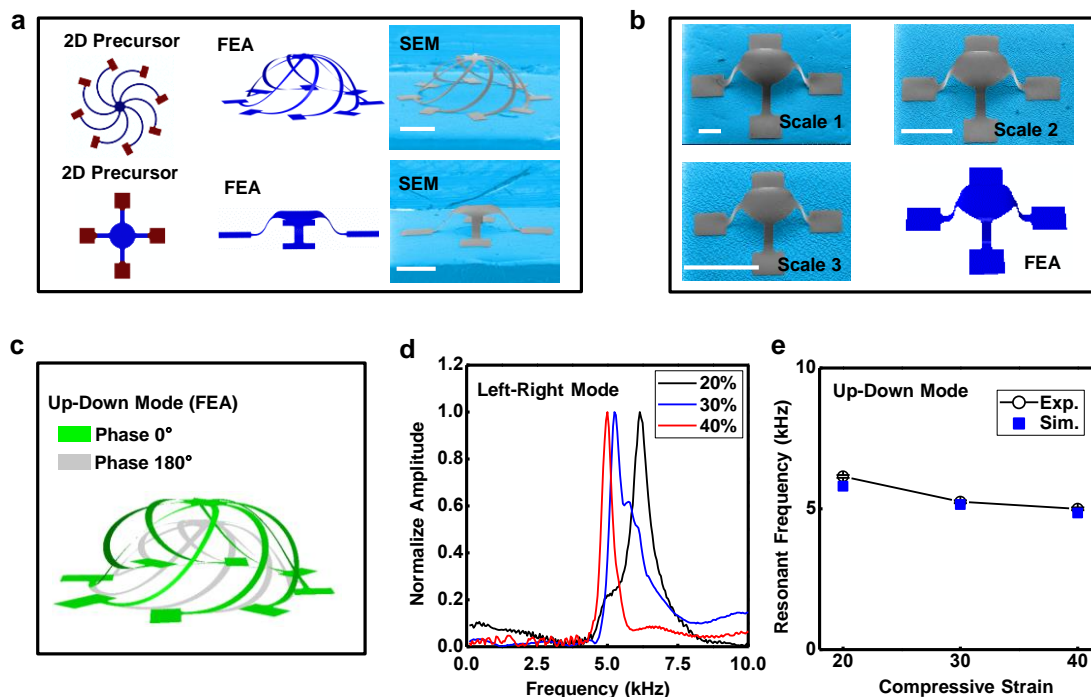


Figure S1. a) 2D precursors, SEM and FEA images of cage and table structures. Scale bar: 500 μm . b) SEM and FEA images of table structures at three scales. Scale bar: 500 μm . c) FEA images of the up-down vibration modes of cage (both the structures and the vibration amplitudes are amplified). d) Measured amplitude-frequency responses of up-down vibrational mode for cage structures. e) Comparison between measured and simulated resonant frequencies of the up-down mode for cage structures.

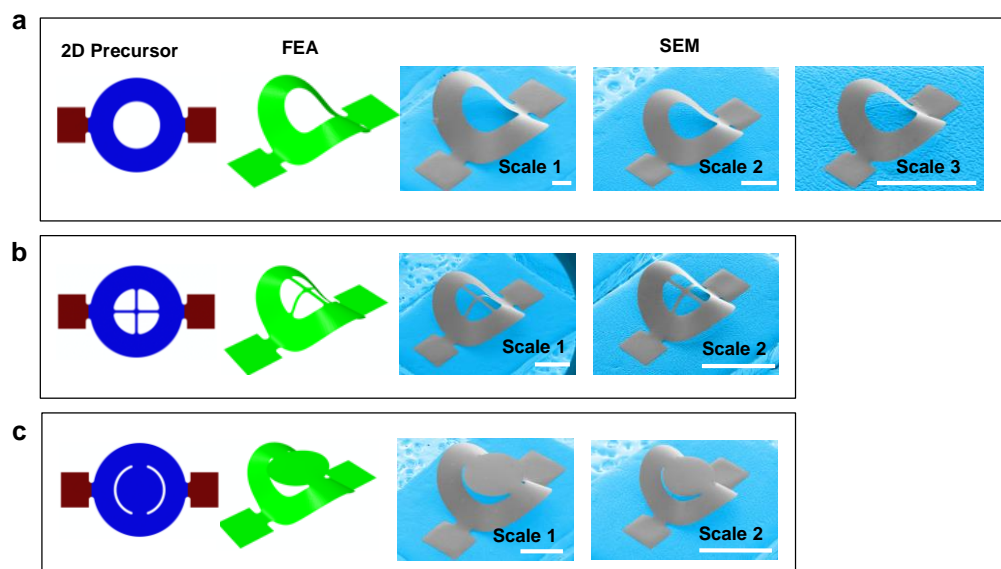


Figure S2. 2D precursors, SEM and FEA images of a) ring structures at three scales (Scale bars: 500 μm), b) ring-cross structures at two scales (Scale bars: 1 mm), and c) ring-disk structure at two scales (Scale bars: 1 mm).

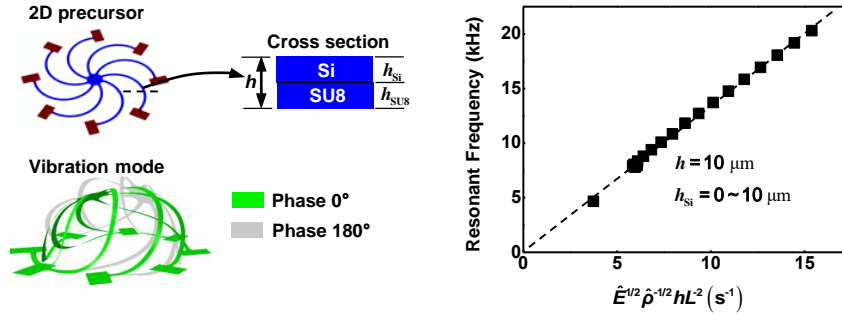


Figure S3. Demonstration of scaling laws for composite structures by FEA. The total thickness is fixed to be $10 \text{ } \mu\text{m}$ and the thickness of the silicon changes from 0 to $10 \text{ } \mu\text{m}$. The FEA simulations show that the resonant frequency linearly depends on the parameter combination $\hat{E}^{1/2} \hat{\rho}^{1/2} h L^{-2}$, where h is the total thickness L is the lateral size, \hat{E} and $\hat{\rho}$ are the equivalent modulus and density respectively, which are expressed by Eq. (1) and Eq. (2) in the main text.

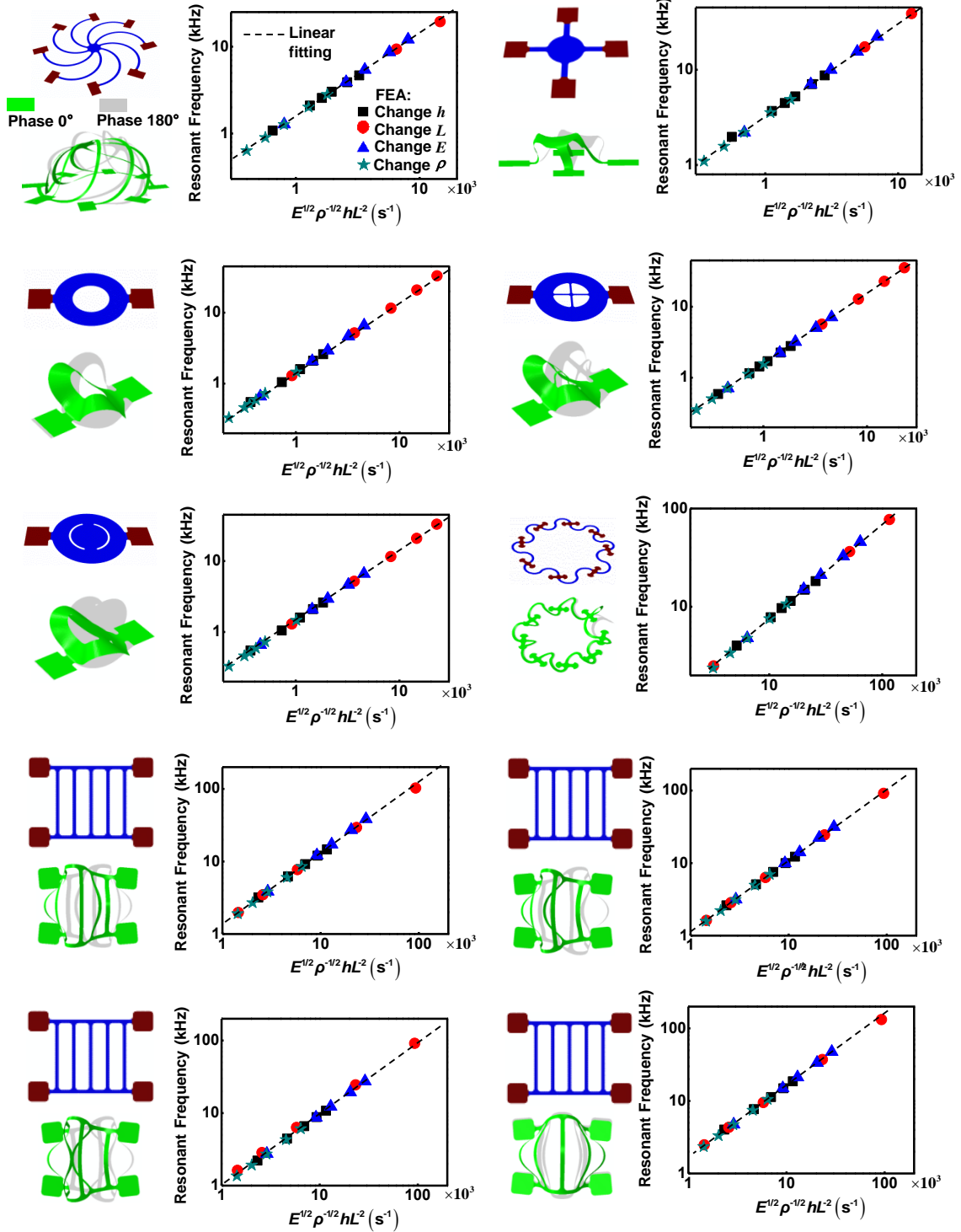


Figure S4. Demonstration of scaling laws by FEA. In the FEA simulations, one of the four parameters (thickness h , lateral size L , modulus E and density ρ) changes at a time while others are fixed. The resonant frequency depends linearly on the parameter combination $E^{1/2} \rho^{-1/2} h L^{-2}$.

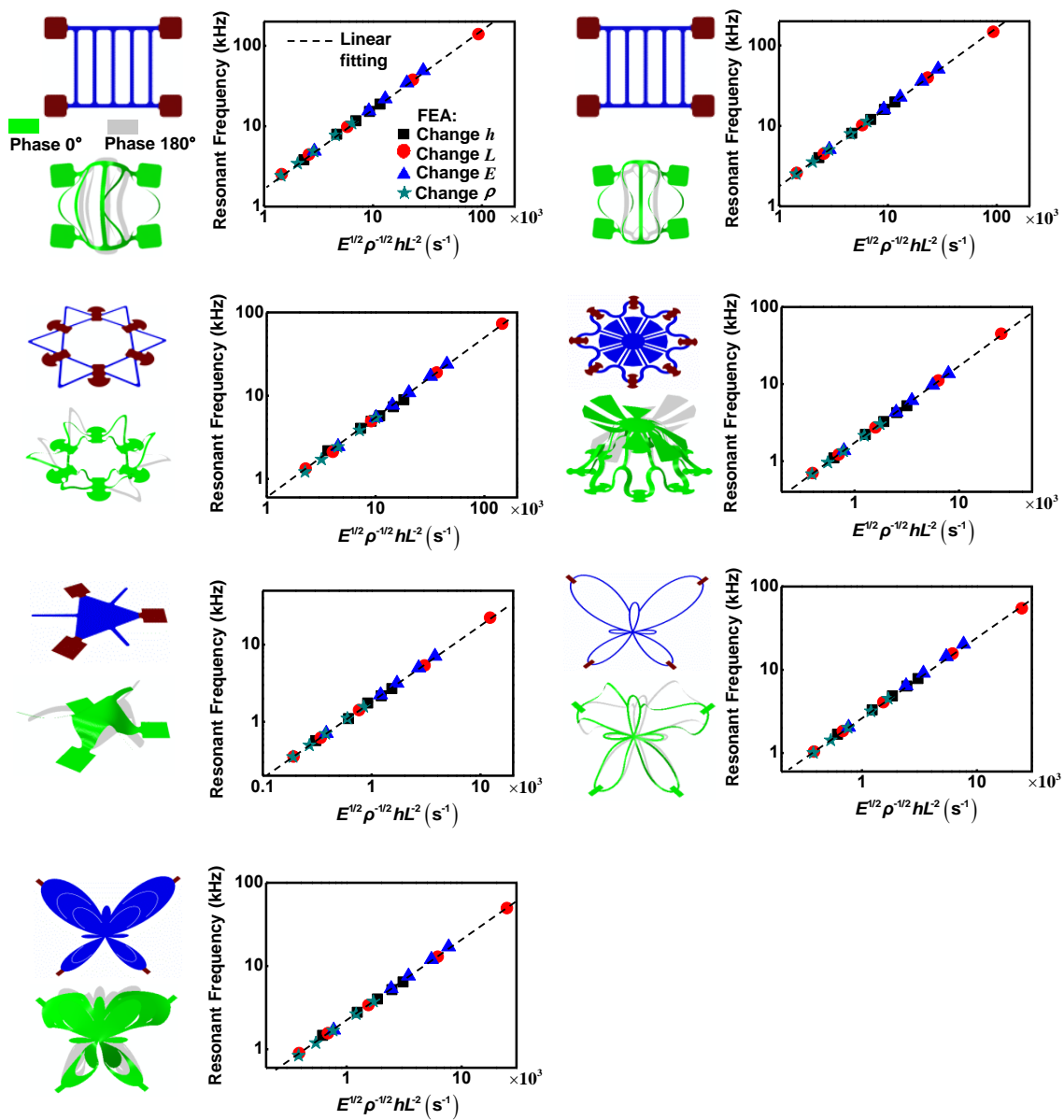
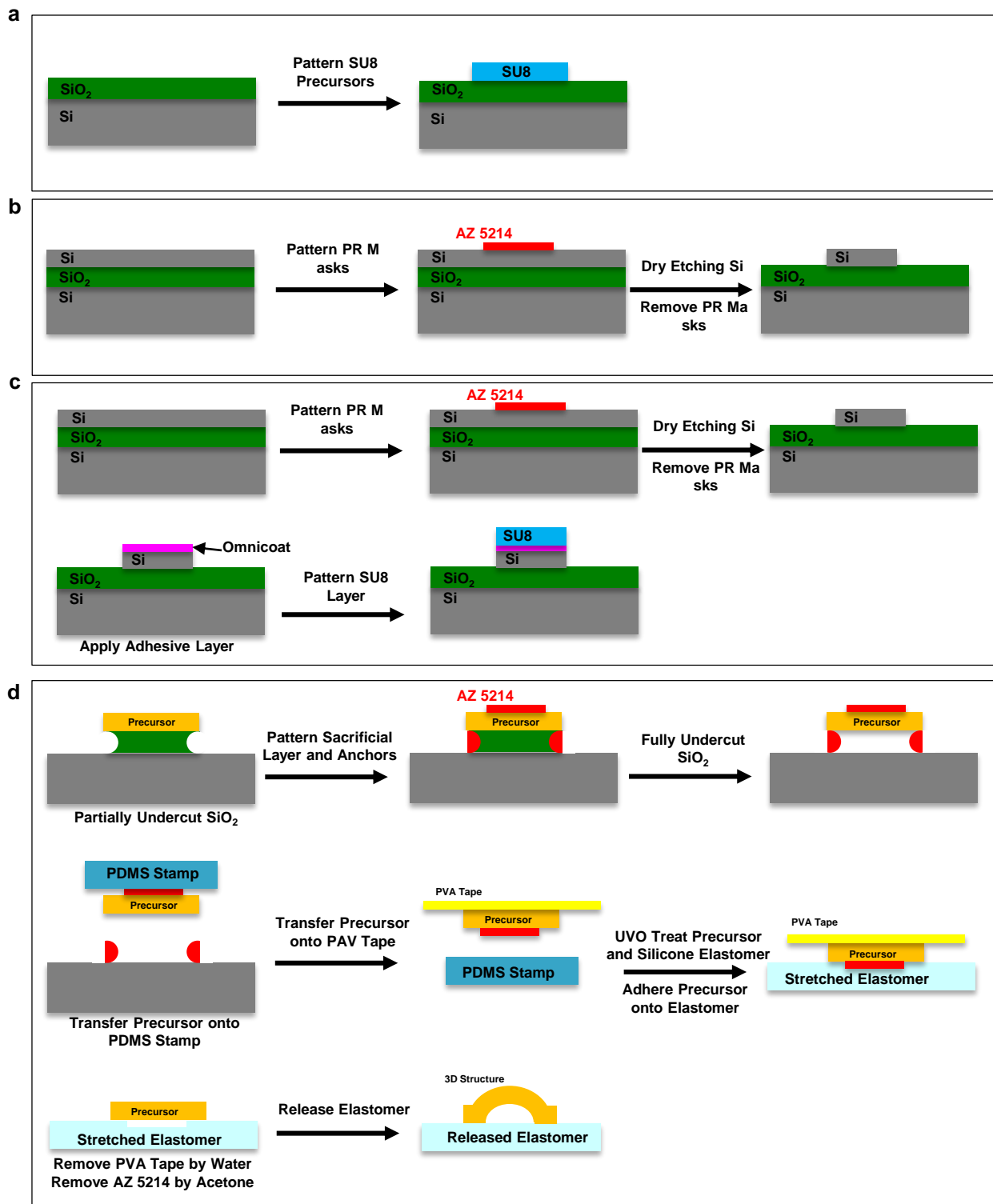


Figure S5. Demonstration of scaling laws (continued).



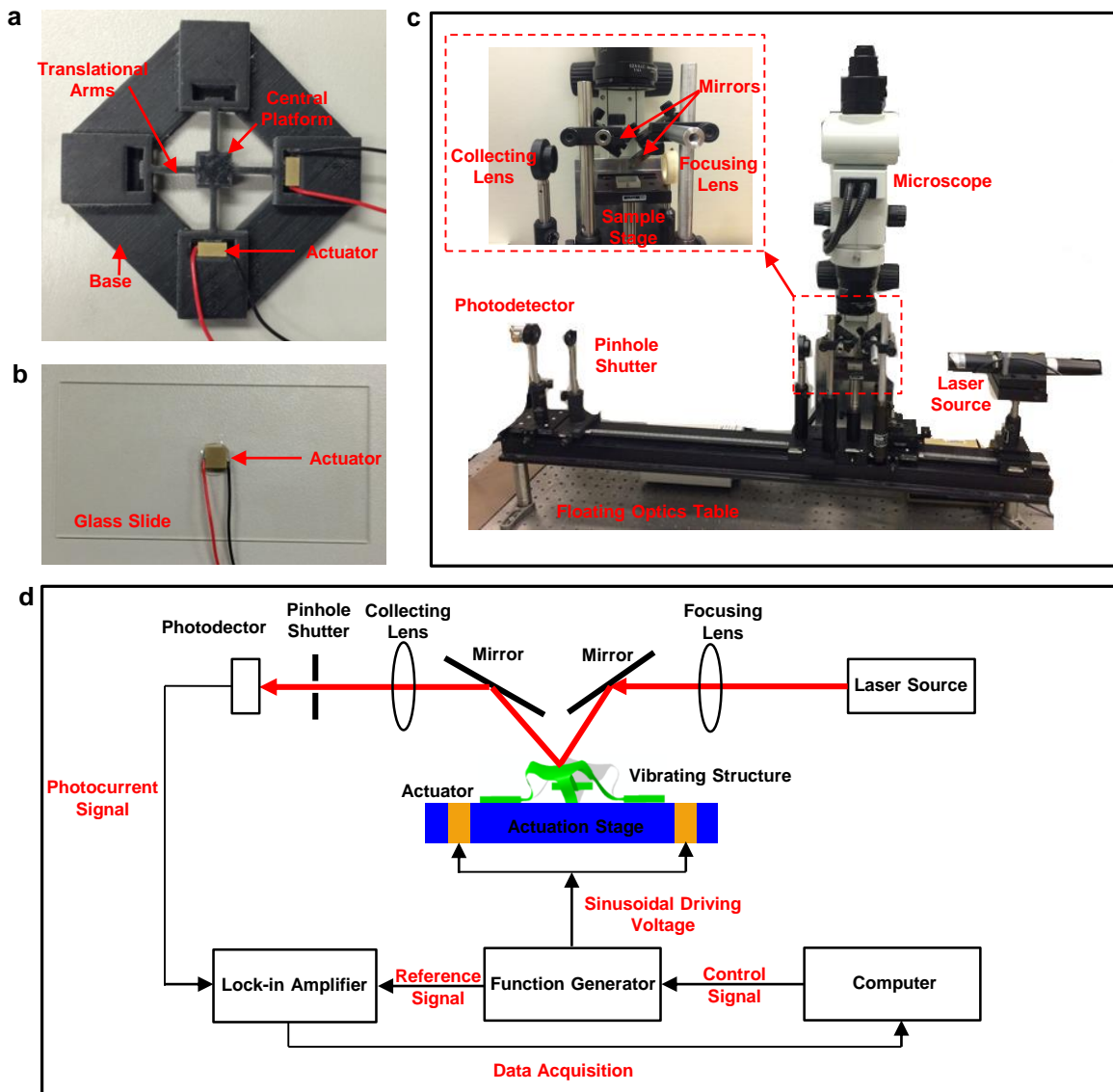


Figure S8. Actuation and measurement systems a) Actuation Stage for X- and Y- actuation. b) Piezoelectric actuator for Z-direction actuation. The Actuator was glued on a piece of glass slide by epoxy. c) Laser system for measure resonant frequencies of 3D structures. d) Schematic of the actuation and measurement system.